Production of Co-58m in a siphon-style liquid target on a medical cyclotron

Mues genannt Koers, L.; McNeil, S. W.; Radchenko, V.; Paulssen, E.; Hoehr, C.

Important note
To cite this publication, please use the final published version (if applicable).
Please check the document version above.

Production of Co-58m in a siphon-style liquid target on a medical cyclotron

L. Mues genannt Koers [a,b], S.W. McNeil [a], V. Radchenko [a,b], E. Paulssen [e,f], C. Hoehr [a,c,d,*]

[a] *Life Sciences Division, TRIUMF, 4004 Wesbrook Mall, Vancouver, BC, V6T2A3, Canada*
[b] *Department of Chemistry, University of British Columbia, 2036 Main Mall, Vancouver, British Columbia, V6T 1Z1, Canada*
[c] *Department of Physics and Astronomy, University of Victoria, 3800 Finnerty Road, Victoria, British Columbia, V8P 5C2, Canada*
[d] *Department of Computer Science, Mathematics, Physics and Statistics, University of British Columbia Okanagan, 3187 University Way, Kelowna, British Columbia, V1V 1V7, Canada*
[e] *Department of Chemistry and Biotechnology, FH Aachen - University of Applied Sciences, Heinrich-Mußmann-Straße 1, Germany*
[f] *Delft University of Technology, Department Radiation Science and Technology, Mekelweg 15, 2629JB Delft, the Netherlands*

ARTICLE INFO

ABSTRACT

We present the production of ^{58m}Co on a small, 13 MeV medical cyclotron utilizing a siphon style liquid target system. Different concentrated iron(III)-nitrate solutions of natural isotopic distribution were irradiated at varying initial pressures and subsequently separated by solid phase extraction chromatography. The radio cobalt ($^{58m/g}$Co and ^{56}Co) was successfully produced with saturation activities of (0.35 ± 0.03) MBq μA^{-1} for ^{58m}Co with a separation recovery of (75 ± 2) % of cobalt after one separation step utilizing LN-resin.

1. Introduction

According to the World Health Organization (WHO) (WHO'Cancer', 2022), cancer is worldwide a leading cause of death with around 10 million deaths in 2020 alone. Therefore, development and improvement of novel treatments against cancer is of vast interest. To help with this problem, internal radionuclide therapy (or targeted radionuclide therapy, TRT) is increasingly gaining interest for cancer therapy (Radchenko and Hoehr, 2020).

In TRT, a radionuclide (mostly emitting corpuscular radiation such as beta-minus (β^-), alpha (α) or Meitner-Auger-Electron (MAE) emitter) typically get attached to a biological vector agent transporting the radionuclide into the proximity of the tumor where it gets accumulated. During the decay of the radionuclide, the emitted particle can inflict lethal damage to the surrounding tumor tissue. But irradiating tumor cells always causes collateral damage to surrounding healthy tissue. To keep the therapeutic index as large as possible - minimizing exposure of healthy tissue and the subsequent side effects while still effectively killing the cancer cells - a precise tailoring of the injected pharmaceutical containing a suitable radionuclide and vector agent is required. To decrease the inevitable irradiation of healthy tissue during tumor treatment, short range, high linear energy transmission (LET) radiation like alpha particles (Ra-223, Ac-225) or Meitner-Auger electrons (In-

111, I-123) are gaining in interest over the past decade (Filosofov et al., 2021; Thisgaard et al., 2011a; Kim and Brechbiel, 2012).

The development of suitable radiopharmaceuticals not only depends on the physical (emissions type, half-life, production cross section) and chemical (solubility, corrosive behavior, acidity) properties of the radionuclide, but on their availability as well. Therefore, new or optimized methods are crucial to enable the production of a vast variety of radionuclides at readily accessible production facilities are.

Conventionally, heavier radiometals are produced via solid target irradiation setups either in a reactor or particle accelerator. These solid target systems often require a large setup or come with high implementation costs for necessary infrastructure which is rarely available in smaller production facilities. Low energy medical cyclotrons, containing liquid target systems, are common in facilities around the globe. They are required for the production of [^{18}F]FDG, the most common radiopharmaceutical for Positron-Emission-Tomography (PET) (Mattos et al., 2001). Therefore, to use already available infrastructure, the production of radiometals in liquid target setups has become more and more desirable over the last decade (Alves et al., 2017; Hoehr et al., 2012a; IAEA, 2019; Hoehr et al., 2012b; IAEA, 2021; Pandey et al., 2019; Pandey and DeGrado, 2020). Up to now, the production of Meitner-Auger electron emitters, for therapeutic purpose, in a liquid target setup is not reported.

To advance the production of precisely tailored radiopharmaceuticals for TRT, this study demonstrates the production of the MAE-emitter ^{58m}Co at a small medical cyclotron utilizing a liquid target system.

^{58m}Co can be produced in multiple ways (Barrett et al., 1235). In this study we focus on low energy (12 MeV) proton capture reaction from an iron target (^{58}Fe(p,n)^{58m}Co). For the reaction with enriched ^{58}Fe, only ^{58g}Co is expected as by product. The cross-section of this reaction is presented in Table A1.

The metastable isotope ^{58m}Co has a half-life of 9.10 h. It decays entirely via internal transition into its ground state ^{58g}Co which further decays into the stable isotope ^{58}Fe (IAEA Nuclear Data Section, 2021). ^{58g}Co has a half-life of 70.86 d, decaying via electron capture as well as positron emission (IAEA Nuclear Data Section, 2021). A decay scheme of ^{58m}Co and ^{58g}Co is presented in Fig. 1.

During the internal transition of ^{58m}Co, up to 6 MAE can be emitted (ENSDF Decay Data) enabling the application as MAE emitter in TRT. The emission yields and energies of the MAE are presented in the Appendix in Table A2.

Previous publications demonstrated the production of ^{58m}Co in a solid target setup (Barrett et al., 1235; Valdovinos et al., 2017; Thisgaard et al., 2011b). ^{58m}Co showed good potential for MAE-therapy specially in combination with the PET nuclide ^{55}Co for theragnostic approaches. It was further shown that rapid post irradiation processing is mandatory to produce ^{58m}Co, since its daughter nuclide ^{58g}Co ($t_{1/2} = 70.86$ d) is active as well, decreasing the radionuclide purity of the product and potentially increasing unnecessary dose uptake of the patient (Thisgaard et al., 2011b).

Liquid target production of radionuclides with short half lives showed tremendous success over the last few decades. ^{18}F ($t_{1/2} = 109.77$ min) and ^{68}Ga ($t_{1/2} = 67.71$ min) (IAEA Nuclear Data Section, 2021) are two examples for commercially used radio nuclides produced in a liquid target set up (Mattos et al., 2001; IAEA, 2019). Therefore, the liquid target setup might be nicely suitable to produce ^{58m}Co for therapeutic purposes.

In this study a so called siphon style liquid target was used. A siphon target possesses as secondary chamber beside the target chamber where the target solution is irradiated. This secondary chamber called expansion chamber is connected to the target chamber and can be filled with He gas to manipulate the pressure inside the target chamber. Further description of a siphon target are presented by Hoehr et al., (2012) (Hoehr et al., 2012a) and Lowis et al., 2021 (Lowis et al., 2021).

To enable future application of radionuclide production at small cyclotron facilities, encountered challenges and necessary preliminary works are discussed (Alves et al., 2017; Hoehr et al., 2012a; IAEA, 2019; Hoehr et al., 2012b; IAEA, 2021; Pandey et al., 2019; Pandey and DeGrado, 2020; Oehlke et al., 2015). We further demonstrate the application of siphon style target systems for radionuclide production.

2. Materials and methods

2.1. Chemicals

Starting materials for the production of ^{58m}Co/^{56}Co, ^{nat}Fe(NO$_3$)$_3$ · 9 H$_2$O (ACS grade) were purchased from Sigma Aldrich (Oakville, Ontario Canada). To prepare the target solution, HNO$_3$ (analytical grade) purchased from Sigma-Aldrich was used without further purification. Deionized water was provided by a Millipore system (Direct-Q® 3UV). To increase the solubility of the salt, the solution was stirred and mildly heated using a Corning pc-420D magnetic stirrer and heater. All weighing was performed on an analytical balance from Mettler Toledo ± 1 mg (Switzerland).

To purify the produced radio cobalt from the iron target solution, solid phase extraction chromatography was performed with LN resin (100–150 μm) and DGA resin purchased from Triskem (Bruz, France) and Eichrom (Chicago, USA), respectively. HCl (analytical grade) used to elute the iron from the column was obtained from Sigma-Aldrich.

2.2. Analytical methods

2.2.1. Chemical purity

The exact metal content of all used target solutions as well as the elemental composition of performed separation experiments were analyzed using an Agilent Technologies 8900 Triple Quad inductively coupled plasma mass-spectrometer (ICP-MS) equipped with an Agilent SPS 4 Autosampler by comparing the sample solution (diluted to 10–100 ppb) to a multi-element standard solution (Agilent Technologies, California USA, Standard 2A).

2.2.2. Radionuclide purity

Radionuclide purity of all product solutions was assessed and quantified by a Canberra N-type High Purity Ge (HPGe) gamma spectrometer (Mirion Technologies, Atlanta USA serial) operated with Genie™ 2000 software and calibrated (energy and efficiency) with 20 mL liquid scintillation (LSC) vials or 1.5 mL HPLC vials containing ^{152}Eu at different distances to the detector. All samples were measured 30 min with an approximate dead time of less than 5%. Sample sizes of 100–1500 μL (diluted to 1500 μL final volume) where taken using an automatic Eppendorf pipette.

2.3. Preparation of target solution

All target solutions were prepared by dissolving iron nitrate salt (Fe(NO$_3$)$_3$ 9H$_2$O) of natural abundance either in Milli-Q water or 1 M HNO$_3$. The natural isotopic distribution present in the salt is presented in Table 1. The solutions were mildly stirred and heated to 50–60 °C to increase solubility. The composition of the target solutions used, measured with ICP-MS, is listed in Table 2. For most of the irradiations, ^{56}Fe was used to produce ^{56}Co which is easier to handle and to detect due to its longer half-life (77.236 d) and better gamma emission (846.8 keV) (IAEA Nuclear Data Section, 2021).

Fig. 1. Decay scheme of ^{58m}Co into the stable ^{58}Fe. Data from (IAEA Nuclear Data Section, 2021).

Table 1

Isotopic composition of natural metal samples (IAEA Nuclear Data Section, 2021). The isotopes of interest for the radionuclide production of this study are marked **bold**.

Iron nuclide	Natural abundance [%]
^{54}Fe	5.85
^{56}Fe	**91.75**
^{57}Fe	2.12
^{58}Fe	**0.28**

Table 2

Presentation of the prepared target solutions and the measured metal concertation. Samples were prepared in 30 mL batches. *These solutions decomposed several days after preparation and could not be measured with ICP-MS. The determination of the concentration was performed after the irradiations were done. The solutions without measured concentration were further processed using the theoretical concentrations. A reason for decomposition was not found.

Iron concentration [M]	Iron concentration [g L^{-1}]	Medium	Metal-Nitrate content [g]	Measured Concentration [g L^{-1}]	Uncertainty [%]
2.5	140	H_2O	30.54	142	1.7
3	168	H_2O	36.72	174	0.9
3.5*	196	H_2O	42.45	–	–
2.5*	140	1 M HNO_3	30.30	–	–

2.4. Theoretical calculation

2.4.1. Yield calculations

To enable an evaluation of the experimentally obtained results, theoretical calculations of potential achievable activities using stopping power tables provided by the SRIM software (SRIM, 2013) and energy dependent (p,n) reaction cross-sections provided by the TENDL nuclear data library (Koning et al., 2019) were carried out. The energy profile along the penetration depth (calculated with SRIM) was used to define the depth of cylinders in which the energy dropped by 1 MeV. These dimensions where then was used together with the metal concentration of the target solution (Table 2) to calculate the target atom density in each cylinder available for reaction in the corresponding energy range (equations (1) and (2)):

$$N(E) = c \bullet V(E) \bullet h \bullet N_{Av} \tag{1}$$

$$V(E) = A \bullet x(E) \tag{2}$$

with *N(E) number of target atoms* in the cylinder of projectile energy *E*, *c* [mol cm^{-3}] the molar target concentration, *V(E)* [cm^3] the cylinder depth volume, which is defined by the beam area *A* [cm^2], *x(E)* the penetration depth of the projectile in [cm], *h* the natural abundance of the target isotope and N_{Av} [mol^{-1}] the Avogadro constant.

In combination with the reaction cross section and the proton flux applied to the target, the expected saturation activity was determined in the step size of 1 MeV and summed up over the range of the proton range to the threshold energy of the corresponding reaction (equations (3)–(5)).

$$A_{sat} = \frac{Y}{\varphi} \tag{3}$$

$$Y = \sum Y(E) \tag{4}$$

$$Y(E) = N(E) \bullet \sigma(E) \bullet \varphi \bullet \left(1 - e^{-\frac{\ln(2)t}{t_{\frac{1}{2}}}}\right) \tag{5}$$

where A_{Sat} is the saturation activity [Bq μA^{-1}], *Y* is the production yield [Bq], φ is the proton beam current [μA], $\sigma(E)$ is the energy dependent cross section [barn], *t* is the irradiation time [s], $t_{1/2}$ is the half-life of the product nuclide [s] and φ is the proton flux [(s cm^2)$^{-1}$]. For all theoretical calculations, it was assumed that the number of target atoms and the proton flux stay constant over the course of the production and do not significantly decrease due to reaction with a target nuclide. The ramp up time of the beam current was neglected for the theoretical calculations, since for the majority of the irradiations, the beam current was stable after a few seconds.

2.4.2. ^{58m}Co activity

Due to the low energy emission of ^{58m}Co (24.9 keV) (IAEA Nuclear Data Section, 2021), it is difficult to measure this nuclide with a conventional gamma spectrometer. To quantify the actual amount of ^{58m}Co produced during an irradiation of ^{58}Fe, the mother-daughter relation of ^{58m}Co to ^{58g}Co was used. As presented by Thisgaard et al. (2011a), the decay of the short-lived mother nuclide (^{58m}Co) into its longer living daughter (^{58g}Co) leads to an accumulation of the daughter nuclide. This

accumulation was calculated by the quantification of ^{58g}Co at two distinct times after the irradiation (at 0 and at *t*) according to equation (6).

$$A_{Co58m}(0) = \left(A_{Co58g}(t) - A_{Co58g}(0) \bullet e^{-\lambda_{Co56} \bullet t}\right) \bullet \frac{\lambda_{Co58g} - \lambda_{Co58m}}{\lambda_{Co58g} \bullet \left(e^{-\lambda_{Co58m} \bullet t} - e^{-\lambda_{Co58g} \bullet t}\right)} \tag{6}$$

Where $A_{Co58m}(0)$ and $A_{Co58g}(0)$ are the activities at EOB of ^{58m}Co and ^{58g}Co respectively. $A_{Co-58g}(t)$ the activity of ^{58g}Co after time t. λ is the decay constant of respective nuclide and t is the time difference between the two measurements.

2.5. Target and irradiation

All irradiations were performed at the TR13, a 13 MeV medical cyclotron at TRIUMF, Vancouver, Canada, with a maximum proton beam current of 10 μA at varying irradiation times between 10 and 20 min and a proton beam of 1 cm diameter. The target body was a siphon style liquid target developed in house (Hoehr et al., 2012a), (Lowis et al., 2021). Different iron solutions containing between 140 and 196 g L^{-1} iron dissolved in Milli-Q water or 1 M HNO_3 were irradiated one to three times (Table 2).

The target was isolated from the cyclotron via double foil He gas-cooled entrance window containing a 25 μm Al foil and a 38 μm HAVAR® foil. The entrance window decreased the proton energy to 12 MeV before entering the target chamber.

To minimize the dose to the experimenter, for some of the experiments the longer living ^{56}Co isotope (77.24 d) (IAEA Nuclear Data Section, 2021) was measured after leaving the product solution for decay for at least one day to decrease the activity of short lived impurities ^{13}N and ^{51}Mn occurring from the irradiation of ^{16}O and ^{56}Fe. For convenience, the yield measurements were performed 20 h and 69 h after End Of Bombardment (EOB).

2.6. Separation measurements

Separation of the produced radiocobalt from the highly concentrated iron target solution was performed with solid phase extraction chromatography (Barrett et al., 1235; Valdovinos et al., 2017). The separation column was loaded with 2.5 g of either LN- or DGA-resin. For conditioning, the column was washed with 5 mL of 1 M HNO_3, discarding the wash solution. Thereafter, an aliquot of 1.5 mL product solution was added. Afterwards, 15 mL of 1 M HNO_3 was added to flush the column and elute all present cobalt (Fraction 1).

To recover the iron target from the column, the column was washed with 4 M HCl for the LN-resin and with 3 M HNO_3 for DGA-resin (Fraction 2).

To prevent radioactive contamination of the mass spectrometer, separation with non-radioactive tracers of respective concentrations were performed.

Each separation was performed once. The separation of the active radio cobalt product was quantified using HPGe gamma spectroscopy, and the separation and recovery of the iron target was measured with ICP-MS (diluted to approximately 50 ppb). The errors were estimated from the gamma spectroscopy and ICP-MS uncertainties.

3. Results and discussion

3.1. Theoretical calculation

To validate the observed experimental results, theoretical calculations regarding the maximum expected production yields and saturation were performed. The theoretical outcomes for the irradiation of different concentrated target solutions are presented in Table 3. The reaction cross sections used for the calculation are presented in the appendix in Table A1.

3.2. Experimental irradiation

To study the influence of different irradiation conditions, the beam current applied to the target as well as the internal target pressure during the irradiation was monitored.

3.2.1. Pressure rise during irradiation – no top-up pressure

Fig. 2 displays a representative current and pressure data set. A correlation between the applied current and the build pressure was observed. In the first 180 s, the current was slowly increased from 0 µA up to 10 µA. In accordance with the current increase, the pressure is rising sharply. Reaching 10 µA, the current stabilized corresponding in a slowing down pressure increase, yet not reaching a constant pressure state.

The steep pressure increase observed during the ramp up of the proton beam is assumed to originate from the increasing heat influx into the target solution, causing a rapid pressure increase as the system is closed. During that phase, a pressure increase of up to 1655 hPa (24 psi) was observed. Once reaching a stable current, the heat exchange between the target and the cooling system equilibrates, causing no further pressure increase. The steady but slow pressure increase observed after 180 s, from 1655 hPa (24 psi) to 1862 hPa (27 psi), can be explained by gas formation due to radiolysis at constant beam current.

Moreover, the inset in Fig. 2 displays a linear regression of the pressure graph between 400 and 500 s into the irradiation. The coefficient of determination (R^2) serves as quantification of the pressure fluctuation inside the target.

The R^2 value is defined in equation (7).

$$R^2 = 1 - \frac{RSS}{TSS} = \frac{\sum (y_i - \widehat{y_i})^2}{\sum (y_i - \overline{y_i})^2} \qquad (7)$$

With RSS is the sum of squared residuals, TSS is the total sum of squares, y_i is the observed value, $\widehat{y_i}$ is the expected value and $\overline{y_i}$ is the mean of all variables.

A R^2 value of 0.0354 was calculated indicating a rather large discrepancy from the linear fitting of the pressure curve in this time section.

Table 3

Theoretical calculations of the saturation activity of different isotopes achievable using the respective target solution. For all theoretical calculations a beam current of 10 µA, a circular beam with a diameter of 1 cm, a natural abundance of Fe-58 of 0.28% and an irradiation time of 10 min was used. The yield at EOB and the A_{Sat} of ^{58m}Co was only measured using 2.5 M solutions.

Target solution	Y at EOB (Co-56) [MBq]	A_{Sat} (Co-56) [MBq/µA]	Y at EOB (Co-58m) [MBq]	A_{Sat} (Co-58m) [MBq/µA]
140 g L^{-1} in H2O	2.04E+03	204.41	3.04	0.304
140 g L^{-1} in HNO3	2.00E+03	199.54	2.97	0.297
168 g L^{-1} in H2O	2.37E+03	237.09		
196 g L^{-1} in H2O	2.71E+03	270.50		

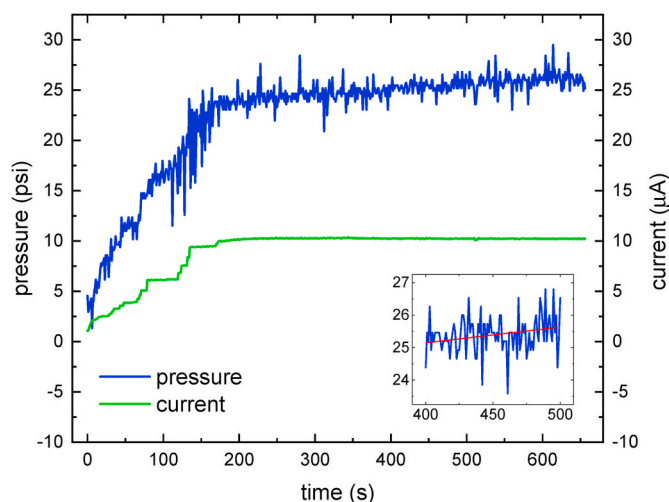**Fig. 2.** Pressure graph of an irradiation of iron(III)nitrate solution containing 140 g L^{-1} iron with natural isotope distribution at normal background pressure (without additional pressure applied), showing the current as well as the pressure inside the target during the irradiation. Furthermore, a linear regression for the pressure 400–500 s into the irradiation is presented in red, indicating a measure of fluctuation of the target pressure. (For interpretation of the references to colour in this figure legend, the reader is referred to the web version of this article.)

As reported previously by Jahangiri et al., (2018) (Jahangiri et al., 2018), these pressure fluctuations might originate from creation of gas bubbles by radiolysis and their constant resorption into the solution. Furthermore, an inhomogeneous distribution of gas bubbles formed in the target chamber and transfer into the expansion chamber can increase those fluctuations of the target pressure.

3.2.2. Pressure rise as a function of metal concentration

To investigate the behavior of the pressure as a function of the metal concentration as well as the ambient solvent of the irradiated solution,
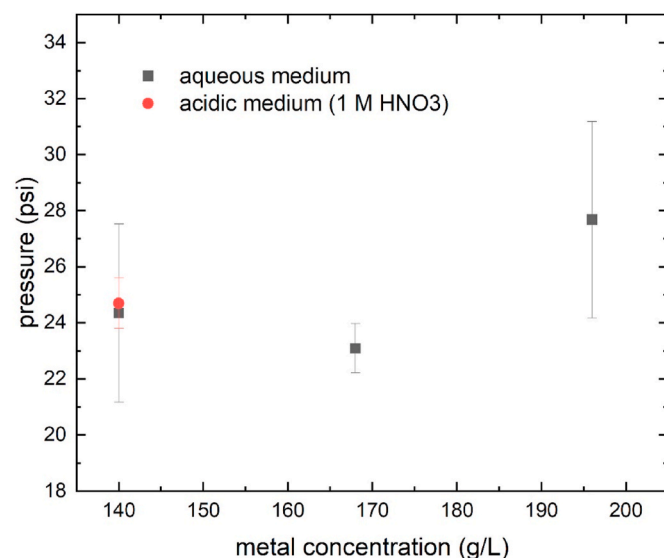

Fig. 3. Comparison of the pressure increase inside the target chamber 10 min into the run for irradiation of target solutions containing different metal concentrations as well as varying solvent (H$_2$O or 1 M HNO$_3$). For all solutions prepared in H$_2$O, at least two measurements were taken. The error bars show the standard deviation of the average of those measurements. For the solution containing HNO$_3$, the error shows the uncertainty of the activity measurement with HPGe gamma spectrometry since only one irradiation was performed.

the increase in pressure after 10 min was measured. The results are displayed in Fig. 3.

In this figure, a weak dependency of pressure increase on the target concentration is shown. The solution with the highest metal content yielded the largest increase in pressure 10 min into the irradiation while the lowest pressure increase was observed irradiating the lowest concentrated target solution.

Moreover, additional nitric acid at similar concentration showed no influence on the pressure increase inside the target chamber. This observation deviates from previous publications investigating liquid target behavior, where the addition of nitric acid lowered the pressure rise (Zacchia et al., 2020; Pandey et al., DeGrado). However, only one irradiation of target solution containing additional nitric acid was performed, which does not give any information about the reliability of this observation.

3.2.3. Pressure rise as a function of initial top-up pressure

In Fig. 4, the influence of the initial pressure on the pressure increase during an irradiation is presented.

While the effect of the target concentration onto the pressure increase, as presented in Fig. 3, is rather weak, variation in the initial pressure showed significant influence on the target behavior. A vast increase of target pressure can be observed, when initial top-up pressure was applied to the expansion chamber of the siphon style target, suggesting that during the irradiation, more gas is produced if initial pressure is applied.

The behavior of the target pressure during an irradiation at increased initial target pressure is presented in Fig. 4. Similar to Fig. 2, during the beam ramp up in the beginning of the irradiation, the target pressure increases rapidly about 1379 hPa (20 psi), afterwards, under stable beam, the pressure increase slowed down. While this observation is similar for irradiations with and without additional pressure, the slow down at higher pressure is significantly less than at lower overall pressure. A slope of approximately 6.9 hPa s^{-1} (0.1 psi s^{-1}) was observed at around 1.7×10^4 hPa (250 psi) target pressure, whereas the pressure increase at 1724 hPa (25 psi) target pressure was around 25 times less with approximately 0.3 hPa s^{-1} (0.004 psi s^{-1}). This is in agreement with the observations in Fig. 4.

Additionally, as presented in Fig. 5, the pressure fluctuations at 400–500 s into the run and quantified by the R^2 value is significantly lower at higher overall target pressure. For a top-up pressure of $1.4 \times$

Fig. 5. Target pressure in dependence of the beam current during an irradiation with additional 200 psi initial target pressure. The linear regression for the pressure 400–500 s into the irradiation is presented in red.

10^4 hPa (206.4 psi), a coefficient of determination of 0.887 was calculated. This is around 25 times more precise than the R^2 value of 0.0354 observed at the example without initial pressure in Fig. 2.

The accelerated increase of the internal target pressure might be the elevated target pressure forcing formed gas bubbles back into the target solution causing less repression of the solution and enabling more contact to the proton beam to the target solution. Hence, the solution undergoes further dose uptake, enhancing radiolysis inside the target.

Furthermore, the increased overall pressure might shape the gas bubbles formed inside the target into numerous smaller bubbles, distributing more homogenously throughout the target chamber, diminishing the fluctuation of pressure. A similar observation was reported by Jahangiri et al., (2018) (Jahangiri et al., 2018) explaining those observations with boiling-condensation mechanics and beam transport.
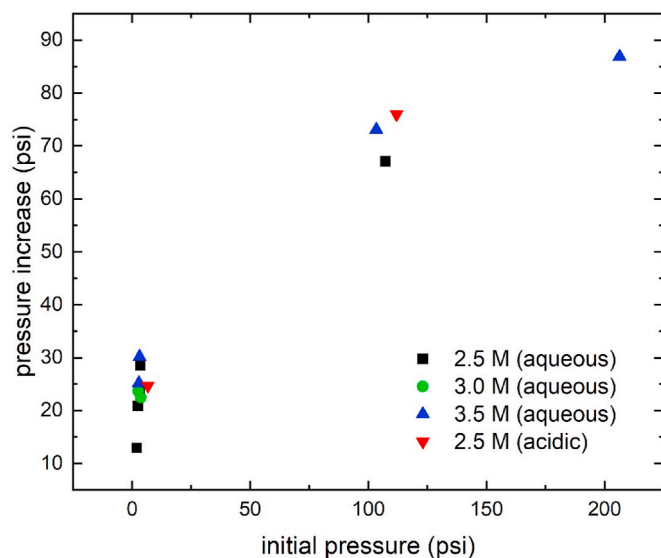

Fig. 4. Showing the pressure increase after 10 min irradiation in dependency of the applied initial pressure on a semi log scale. Presented are four different target solutions of varying target concentration in aqueous and acidic medium.
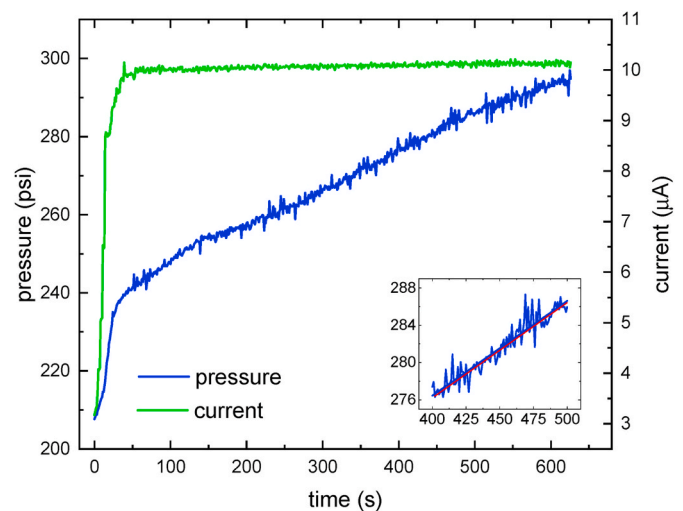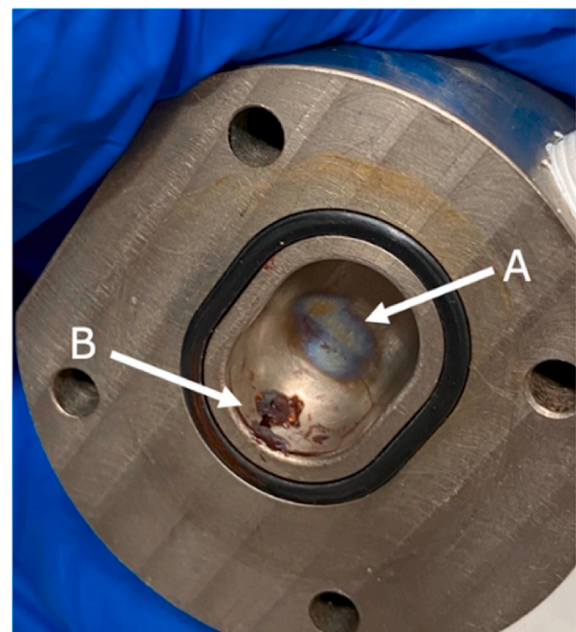

Fig. 6. Picture of the target chamber opened up for maintenance showing blueish colored stain in the back of the chamber (A) and brownish iron sludge in the bottom (B).

This assumption is further supported by the observation presented in Fig. 6, showing the inside of the target chamber, disassembled after an irradiation of the iron target solution. Arrow A marks a colored stain at the back of the target chamber, suggesting material alteration due to beam impact. Theoretical calculation of the beam penetration depth as mentioned in paragraph 2.4 yielded a maximum penetration death of watery solutions of approximately 1.2 mm, whereas the target chamber has a depth of 10 mm making it unlikely that the beam reaches the back of the target without density alterations of the target solution which might be caused by gas formation.

The additionally applied pressure is expected to counter act the evaporation of the target solution causing the solution to be exposed to the proton beam longer resulting in more heat transfer into the solution and in turn leading to higher overall pressure inside the target.

This pressure increase however, revealed an additional problem. Irradiations at elevated target pressure resulted in precipitation of target solution. This precipitate is presented by arrow B in Fig. 6. It was assumed, that the increase in target pressure is caused by an increase in temperature inside the target. This assumption is supported by Elmasry et al., (1998) reporting the formation and precipitation of iron(III)oxide (Fe_2O_3) from iron(III)nitrate at 523 K (Elmasry et al., 1998) and further confirmed by observation of sludge formation after heating iron(III)nitrate solution to approximately 300 °C.

Therefore, even though higher target pressure comes with less pressure fluctuations, we decided not to increase the target pressure artificially, to keep the risk of co-precipitating the product as low as possible.

3.3. Radioactivity yield

3.3.1. Radioactive yield of ^{56}Co

The production yield obtained from measuring ^{56}Co was decay corrected to EOB and corrected for the applied current to achieve the saturation activity A_{Sat} (MBq μA^{-1}). In Fig. 7, the saturation activities obtained from the irradiations without initial pressure are plotted against the integrated current applied to the target solution during the irradiation.

Although the saturation activity is should be independent of the applied beam current and irradiation time, see equation (5), the results presented in Fig. 7 show significant lower saturation activities for longer irradiations than for shorter ones. This observation concours with results previously described by Oehlke et al., (2014) (Oehlke et al., 2015).
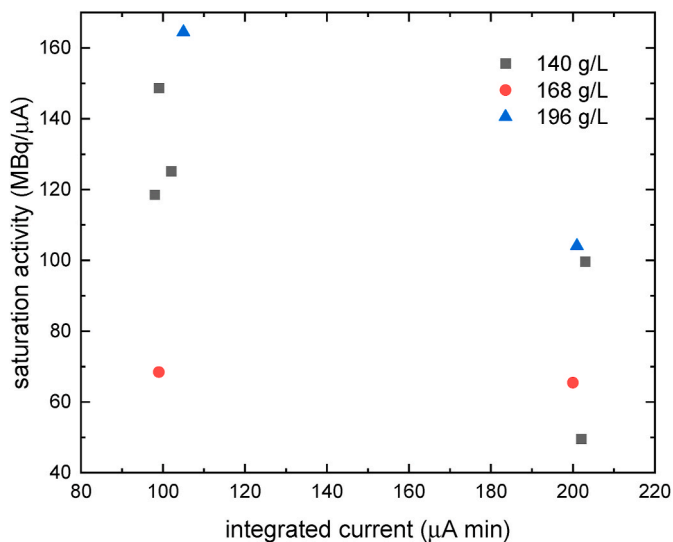
Fig. 7. Display of the saturation activity of different target metal concentrations depended on the integrated current applied to the target solution during irradiation.

Furthermore, a non-linear dependency of the metal concentration of the target solution on the produced saturation activities is presented. The lowest saturation activity was observed irradiating target solutions with intermediate metal content whereas the highest saturation activity was found for target solutions with the highest metal content.

Considering that more concentrated solutions possess higher target atom densities, it is expected, that the saturation activity scales with the metal concentration of the target solution (disregarding small changes in the penetration range of the proton beam). This assumption differs from previous publications of Oehlke et al., (2015) (Oehlke et al., 2015) presenting lower saturation activities for higher concentrated target solutions as well, which is in accordance with the decrease of the saturation activity from the solution concentration of 140 g L^{-1} to 168 g L^{-1} solutions, however not the subsequent increase to the 196 g L^{-1} solutions.

During irradiations with additional initial pressure, saturation activities between 178.9 and 376.7 MBq μA^{-1} were measured which are up to twice as high as without initial pressure. However, as described before, irradiations at overall higher pressure resulted in formation of precipitate impeding the product delivery and sample preparation.

A validation of the production yield of irradiations without initial pressure was obtained by comparison of the measured saturation activities with the calculated theoretical values (Table 4).

In most irradiations, the observed production yield was lower than the theoretical calculated value. These observations can be connected to the overall low target pressure and the rather high-pressure fluctuations explained by the formation of gas bubbles (section 3.2.1), further suggesting that not all target atoms were present in the beam trajectory for nuclear reaction.

Overall, the measured saturation activities show a weak concentration dependency, are (against expectations) decreasing over longer irradiation times and are lower than the theoretically expected activities. Still, significant amounts of ^{56}Co were produced.

3.3.2. Radioactive yield of ^{58m}Co

The quantification of ^{58m}Co produced during the irradiation was performed by measuring the accumulation of its daughter nuclide ^{58g}Co over a time as described in section 2.4, equation (6).

The obtained activities of ^{58m}Co are presented in Table 4. It is shown, that the produced activity of ^{58m}Co is slightly higher than the calculated theoretical expectations.

This can be explained since only the standard deviation of the measurement was used for the error estimation. However, additional errors may have been underestimated that can occur during the recovery

Table 4

Overview of the produced activities at different target concentrations and different irradiation times compared to the theoretically calculated expectation values. The error of the measured saturation activities was estimated by calculating the standard deviation of three irradiations under identical conditions (140 g L^{-1}, 10 min irradiation) and applying the relative deviation to the other irradiations.

Product	Target metal conc. [g L^{-1}]	Irradiation time [min]	Measured Saturation Activity [MBq μA^{-1}]	Theoretical Saturation Activity [MBq μA^{-1}]	Relative yield (Measured/ Theoretical) [%]
Co-56	140	10	131 ± 15.8	204	66
	140	20	74.6 ± 9.0	204	40
	168	10	68.4 ± 8.3	237	27
	168	20	65.5 ± 7.9	237	27
	196	10	164.5 ± 19.9	271	61
	196	20	104.1 ± 12.6	271	38
Co-58m	140	10	0.35 ± 0.03	0.315	109

of the product and the preparation of the samples.

3.4. Chemical separation

The separation of the irradiation product from the target solution is mandatory for further processing as well as recycling of potentially enriched target solutions. The separation of cobalt from iron utilizing solid phase extraction chromatography was previously reported by Thisgaard et al., (2011) (Thisgaard et al., 2011a) and Qaim et al., 2018 (Qaim et al., 2018) using a hydrochloric acid solvent. However, Oehlke et al., 2015 (Oehlke et al., 2015) observed corrosive behavior of metal chloride solutions against the HAVAR® foil sealing the target chamber. This was further confirmed by tests orchestrated prior to this study by boiling HAVAR® foil in hydrochloric as well as nitric acid and measuring the alteration of the foil gravimetrically, showing strong alteration of the HAVAR® foil in hydrochloric ambient but not for nitric acid. Therefore, a solid phase extraction chromatography in nitric acid was investigated.

As extraction resins, LN-resin and DGA-resin were investigated. For both resins, a strong affinity to bind to iron was reported. However, the adsorption of cobalt is negligible in 1 M nitric acid (Pourmand and Dauphas, 2010) leading to the assumption that for both resins cobalt would not bind to the column but rather elute immediately (Fraction 1) whereas most of the iron should remain bound to the column. Afterwards, the iron can be eluted by using 4 M HCl for LN-resin and 3 M HNO_3 for DGA-resin (Fraction 2) (Pourmand and Dauphas, 2010; Burnett et al., 1995).

After the first separation, promising separation efficiencies were already observed. The results of this investigation are presented in Table 5. For the separation using LN-resin, (75 ± 2)% of the starting activity was measured in the first fraction while containing (2.0 ± 0.1)% of the initial iron concentration. The DGA-resin showed similar results separating (70 ± 2)% of the ^{56}Co containing (1.2 ± 0.1)% of the initial iron concentration as residual impurity from the product solution.

Applying further separation steps with these resins or adding additional columns of resin to one separation run, is expected to further increase the separation efficiency.

The recovery of the iron target solution was performed with 4 M HCl for the LN-resin and 3 M HNO_3 for the DGA-resin. For LN-resin, (64 ± 2)% of the initial iron was recovered, whereas only (11 ± 1)% could be re-eluted from the DGA resin in 20 mL solution.

No activity was measured in either solution recovered from the column.

Regarding the rather low recovery rate of the iron solution (specifically for DGA resin) and the change in medium (for LN resin) the recovered solution needs further handling for possible recycling purposes.

4. Conclusion

We demonstrated the production of ^{58m}Co in a liquid target system for the first time by utilizing a siphon-style liquid target system on a 13 MeV cyclotron at TRIUMF. Up to (0.35 ± 0.03) MBq µA^{-1} ^{58m}Co was produced from iron-nitrate solutions of natural isotope distribution for iron which is around the same order of magnitude as the theoretical calculations for ^{58m}Co of 0.32 MBq µA^{-1}, performed in this work. Aiming for irradiations including enriched target solutions ($>98\%$ ^{58}Fe) saturation activities above 100 MBq µA^{-1} might be achievable under otherwise similar conditions.

Optimization of the irradiation conditions was performed by observation of the target performance showing a weak dependency of the concentration of the target solution. Furthermore, a dependency of the production yield on the internal target pressure was demonstrated.

Potential benefit to the application of the siphon-style target has been shown by an increase in produced activity when applying an initial

Table 5
Separation of cobalt from iron using solid phase extraction chromatography with LN- and DGA-resin. The activities were obtained by analysis with HPGe gamma spectrometry, the non-active metal content was measured using ICP-MS.

Solution	Activity [Bq]	Recovery [%]	Iron Content [g cm^{-3}]	Recovery [%]
Starting solution	18278 ± 292		0.174 ± 2E-3	
Eluate DGA	12739 ± 301	70 ± 2	0.00205 ± 3E-5	1.18 ± 0.02
Eluate LN	13651 ± 292	75 ± 2	0.00343 ± 8E-5	1.97 ± 0.05
Re-eluate DGA	0	0	0.020 ± 3E-3	11.3 ± 1.9
Re-eluate LN	0	0	0.111 ± 3E-3	63.6 ± 1.6

background pressure inside the target chamber. Maximum of 377 MBq µA^{-1} of ^{56}Co were achieved with an initial pressure of around 6895 hPa (100 psi) compared to the maximum 164 MBq µA^{-1} of ^{56}Co produced without additional pressure. Any application of initial pressure caused precipitation of target solution as side effect. Due to the precipitation, fluid product transfer as well as homogeneous sample preparation are difficult to guarantee, preventing error free determination of produced ^{56}Co. A possible reason for the precipitate formation was investigated by heating the non-irradiated target solution to around 300 °C on a hotplate at which precipitation was observed.

To evaluate the application of ^{58m}Co in medical application, possible separation of radio cobalt from the iron target using solid phase extraction chromatography was presented. Up to (75 ± 2)% of the starting activity with (2.0 ± 0.1)% iron contamination could be separated using LN-resin solid phase extraction chromatography.

CRediT authorship contribution statement

L. Mues genannt Koers: Writing – review & editing, Writing – original draft, Visualization, Validation, Investigation, Formal analysis, Data curation, Conceptualization. **S.W. McNeil:** Writing – review & editing, Investigation, Formal analysis. **V. Radchenko:** Writing – review & editing, Supervision, Project administration. **E. Paulssen:** Writing – review & editing, Supervision, Funding acquisition. **C. Hoehr:** Writing – review & editing, Writing – original draft, Visualization, Validation, Supervision, Project administration, Methodology, Funding acquisition, Formal analysis, Conceptualization.

Declaration of competing interest

The authors declare that they have no known competing financial interests or personal relationships that could have appeared to influence the work reported in this paper.

Data availability

Data will be made available on request.

Appendix

Table A1
Cross-section of proton reactions with Fe-58 to produce different Co-species at proton energies between 1 and 12 MeV (Koning et al., 2019).

Energy [MeV]	Fe-58 (p, X) Co-58m [mb]	Fe-56 (p, X) Co-56 [mb]
12	196.00	383.17
11	183.95	371.06
10	163.67	351.15
9	141.29	329.51
8	116.36	297.06
7	89.27	216.17
6	61.99	80.73
5	36.91	0.00
4	10.72	0.00
3	0.00	0.00
2	0.00	0.00
1	0.00	0.00
Threshold Energy [MeV]	3.2	5.6

Table A2
Emission probabilities and energies of MAE during the internal transition of ^{58m}Co to its ground state ^{58g}Co.

Radiation	Yield [%]	Energy [keV]
Auger-K	12.6	0.75
Auger-L	44.7	6.1
ce-K	73.0	17.2
ce-L	23.5	24.0
ce-M	3.4	24.8
ce-N+	0.1	24.9

References

Alves, F., et al., 2017. 'Cyclotron Production of Ga-68 for Human Use from Liquid Targets: from Theory to Practice', Presented at the WTTC16: Proceedings of the 16th International Workshop on Targetry and Target Chemistry. Santa Fe, NM, USA, 020001. https://doi.org/10.1063/1.4983532.

K. E. Barrett, H. A. Houson, W. Lin, S. E. Lapi, and J. W. Engle, 'Production, purification, and applications of a potential theranostic pair: cobalt-55 and cobalt-58m', Diagnostics, vol. 11, no. 7, p. 1235, Jul. 2021, doi: 10.3390/diagnostics11071235.

Burnett, W.C., Cable, P.H., Moser, R., 1995. Determination of radium-228 in natural waters using extraction chromatographic resins. Radioact. Radiochem. 6 (3).

Elmasry, M.A.A., Gaber, A., Khater, E.M.H., 1998. Thermal decomposition of Ni(II) and Fe(III) nitrates and their mixture. J. Therm. Anal. Calorim. 52 (2), 489–495. https://doi.org/10.1023/A:1010155203247.

'ENSDF Decay Data'. https://www.nndc.bnl.gov/useroutput/58co_mird.html (accessed Mar. 09, 2022).

Filosofov, D., Kurakina, E., Radchenko, V., 2021. Potent candidates for targeted auger therapy: production and radiochemical considerations. Nucl. Med. Biol. 94 (95), 1–19. https://doi.org/10.1016/j.nucmedbio.2020.12.001.

Hoehr, C., et al., 2012a. 'Producing Radiometals in Liquid Targets: Proof of Feasibility with [sup 94m]Tc', Presented at the 14TH INTERNATIONAL WORKSHOP on TARGETRY and TARGET CHEMISTRY. Playa del Carmen, Mexico, pp. 56–60. https://doi.org/10.1063/1.4773940.

Hoehr, C., et al., 2012b. Radiometals from liquid targets: 94mTc production using a standard water target on a 13MeV cyclotron. Appl. Radiat. Isot. 70 (10), 2308–2312, Oct. https://doi.org/10.1016/j.apradiso.2012.06.004.

IAEA, 2019. Gallium-68 Cyclotron Production. IAEA, Vienna. Accessed: Jul. 15, 2022. [Online]. Available: https://public.ebookcentral.proquest.com/choice/publicfullrecord.aspx?p=5812168.

IAEA Nuclear Data Section, 2021. 'Isotope Browser'. IAEA.

IAEA, 2021. Production of Emerging Radionuclides towards Theranostic Applications: Copper-61. Scandium-43 and -44, and Yttrium-86.

Jahangiri, P., Martinez, D.M., Hoehr, C., 2018. Pressure rise in medical cyclotron liquid targets: transient analysis. Appl. Radiat. Isot. 136, 87–100. https://doi.org/10.1016/j.apradiso.2018.01.034.

Kim, Y.-S., Brechbiel, M.W., 2012. An overview of targeted alpha therapy. Tumor Biol. 33 (3), 573–590. https://doi.org/10.1007/s13277-011-0286-y.

Koning, A.J., Rochman, D., Sublet, J.-Ch, Dzysiuk, N., Fleming, M., van der Marck, S., 2019. TENDL: complete nuclear data library for innovative nuclear science and technology. Nucl. Data Sheets 155, 1–55. https://doi.org/10.1016/j.nds.2019.01.002.

Lowis, C., Ferguson, S., Paulßen, E., Hoehr, C., 2021. Improved Sc-44 production in a siphon-style liquid target on a medical cyclotron. Appl. Radiat. Isot. 172, 109675 https://doi.org/10.1016/j.apradiso.2021.109675.

Mattos, D.M.M., et al., 2001. Which are the most used radionuclides in the pet and in the spect techniques in the world? J. Label. Compd. Radiopharm. 44 (S1), S841–S843. https://doi.org/10.1002/jlcr.25804401295.

Oehlke, E., et al., 2015. Production of Y-86 and other radiometals for research purposes using a solution target system. Nucl. Med. Biol. 42 (11), 842–849. https://doi.org/10.1016/j.nucmedbio.2015.06.005.

Pandey, M.K., DeGrado, T.R., 2020. Cyclotron production of PET radiometals in liquid targets: aspects and prospects. Curr. Rad. 13 (Aug) https://doi.org/10.2174/1874471013999200820165734.

Pandey, M.K., Byrne, J.F., Schlasner, K.N., Schmit, N.R., DeGrado, T.R., 2019. Cyclotron production of 68Ga in a liquid target: effects of solution composition and irradiation parameters. Nucl. Med. Biol. 74 (75), 49–55. https://doi.org/10.1016/j.nucmedbio.2019.03.002.

M. K. Pandey, H. P. Engelbrecht, J. F. Byrne, A. B. Packard, and T. R. DeGrado, 'Production of 89Zr via the 89Y(p,n)89Zr reaction in aqueous solution: Effect of solution composition on in-target chemistry', Nucl. Med. Biol., vol 41, no. 4, pp. 309–316, Apr. 2014, doi: 10.1016/j.nucmedbio.2014.01.006.

Pourmand, A., Dauphas, N., 2010. Distribution coefficients of 60 elements on TODGA resin: application to Ca, Lu, Hf, U and Th isotope geochemistry. Talanta 81 (3), 741–753. https://doi.org/10.1016/j.talanta.2010.01.008.

Qaim, S.M., Scholten, B., Neumaier, B., 2018. New developments in the production of theranostic pairs of radionuclides. J. Radioanal. Nucl. Chem. 318 (3), 1493–1509, Dec. https://doi.org/10.1007/s10967-018-6238-x.

Radchenko, V., Hoehr, C., 2020. Modern alchemy to fight cancer. Nucl. Phys. News 30 (2), 28–32. https://doi.org/10.1080/10619127.2020.1752101.

SRIM, 2013. SRIM - the Stopping and Range of Ions in Matter [Online]. Available: www.srim.org.

Thisgaard, H., Elema, D.R., Jensen, M., 2011a. Production and dosimetric aspects of the potent Auger emitter ^{58m}Co for targeted radionuclide therapy of small tumors: production and dosimetric aspects of the Auger emitter Co-58m. Med. Phys. 38 (8), 4535–4541, Jul. https://doi.org/10.1118/1.3608905.

Thisgaard, H., Olesen, M.L., Dam, J.H., 2011b. Radiosynthesis of 55Co- and 58mCo-labelled DOTATOC for positron emission tomography imaging and targeted radionuclide therapy: radiosynthesis of 55Co- and 58mCo-labelled DOTATOC. J. Label. Compd. Radiopharm. 54 (12), 758–762. https://doi.org/10.1002/jlcr.1919.

Valdovinos, H.F., et al., 2017. Cyclotron production and radiochemical separation of 55Co and 58mCo from 54Fe, 58Ni and 57Fe targets. Appl. Radiat. Isot. 130, 90–101. https://doi.org/10.1016/j.apradiso.2017.09.005.

WHO, 'Cancer'. accessed Mar. 09, 2022). https://www.who.int/news-room/fact-sheets/detail/cancer.

Zacchia, N.A., Martinez, D.M., Hoehr, C., 2020. Radiolysis reduction in liquid solution targets for the production of 89Zr. Appl. Radiat. Isot. 155, 108791 https://doi.org/10.1016/j.apradiso.2019.06.037.